Space Weather

RESEARCH ARTICLE
10.1029/2024SW003957

Successively Equatorward Propagating Ionospheric Acoustic Waves and Possible Mechanisms Following the M_w 7.5 Earthquake in Noto, Japan, on 1 January 2024

Bing Zhang[1,2], Tong Liu[2], Xueshang Feng[1], and Guochang Xu[3]

[1]School of Aerospace Science, Harbin Institute of Technology, Shenzhen, China, [2]Department of Land Surveying and Geo-Informatics, The Hong Kong Polytechnic University, Hong Kong, China, [3]Shenzhen Institute of Advanced Technology, Chinese Academy of Sciences, Shenzhen, China

Abstract On 1 January 2024, the M_w 7.5 Noto Peninsula earthquake in Japan generated ionospheric disturbances detected via dense GNSS networks. Significant coseismic acoustic waves emerged ~8 min post-event, exhibiting 0.3 TECU amplitudes, 2–8 min periods, and ~1 km/s propagation speeds. These disturbances propagated exclusively southward as arc-shaped fronts. The observed anisotropy aligns closely with the local geomagnetic field orientation (declination 8.7°), suggesting magnetic channeling as a key factor. Secondary factors likely include northward thermospheric winds suppressing northward wave propagation and land-ocean coupling efficiency differences, which enhanced vertical displacements over southern continental regions. Notably, weak disturbances linked to the M_w 6.2 aftershock were detected, challenging conventional magnitude thresholds for ionospheric detection. While the mainshock's CID dynamics reflect known magnetic guidance mechanisms, the southward preference highlights site-specific interactions between seismic forcing and geophysical filters. This study provides new observational evidence of earthquake-ionosphere coupling, emphasizing the detectability of moderate-magnitude events under favorable conditions, with implications for space weather monitoring and multi-scale seismic hazard assessment.

Plain Language Summary A major earthquake (magnitude 7.5) struck Japan's Noto Peninsula on 1 January 2024, creating ripples not just on the ground but also in Earth's upper atmosphere. Using satellite navigation data, scientists detected unusual electron fluctuations in the ionosphere—a charged atmospheric layer—starting just 8 min after the quake. These disturbances traveled southward in an arc pattern, moving at ~1 km/s. The southward direction matched the alignment of Earth's magnetic field in the region, suggesting the magnetic field acted like a "road" guiding the waves. Differences between land and ocean crust movements and strong high-altitude winds further shaped this pattern. A smaller aftershock (magnitude 6.2) also caused detectable ionospheric ripples, challenging the belief that only larger quakes (magnitude ≥6.6) can do so. This discovery highlights how even moderate earthquakes can leave fingerprints in space, improving our ability to monitor Earth's seismic activity through atmospheric signals.

Key Points:

- M_w 7.5 quake triggered southward-propagating ionospheric waves aligned with geomagnetic field, highlighting magnetic channeling dominance
- Northward thermospheric winds and land-ocean coupling asymmetry may suppress northern CID propagation, enhancing southern arc-shaped fronts
- Weak M_w 6.2 aftershock ionospheric signals defy conventional magnitude limits, proving moderate quakes' detectability

Supporting Information:

Supporting Information may be found in the online version of this article.

Correspondence to:

T. Liu,
tong2.liu@polyu.edu.hk

Citation:

Zhang, B., Liu, T., Feng, X., & Xu, G. (2025). Successively equatorward propagating ionospheric acoustic waves and possible mechanisms following the M_w 7.5 earthquake in Noto, Japan, on 1 January 2024. *Space Weather*, *23*, e2024SW003957. https://doi.org/10.1029/2024SW003957

Received 16 APR 2024
Accepted 27 MAR 2025

Author Contributions:

Conceptualization: Tong Liu
Data curation: Bing Zhang
Formal analysis: Bing Zhang, Tong Liu
Funding acquisition: Xueshang Feng, Guochang Xu
Investigation: Bing Zhang
Methodology: Tong Liu
Project administration: Xueshang Feng, Guochang Xu
Software: Bing Zhang, Tong Liu
Supervision: Xueshang Feng, Guochang Xu
Validation: Bing Zhang, Tong Liu
Visualization: Bing Zhang, Tong Liu

1. Introduction

On 1 January 2024, at 16:10 local time (7:10 UTC), a powerful earthquake measuring M_w 7.5 in magnitude struck the Noto Peninsula in Japan. This seismic event is notable as the largest earthquake to hit Japan since the 2011 Tōhoku M_w 9.0 earthquake that occurred off the Pacific coast. Extensive research has shown that earthquakes can trigger atmospheric disturbances, leading to either direct co-seismic ionospheric disturbances (CIDs or CSIDs) (Astafyeva, 2019; Heki, 2021; Jin et al., 2015) or other types of traveling ionospheric disturbances (TIDs) (Artru et al., 2005; Chou et al., 2022; Rolland, Lognonné, Astafyeva, et al., 2011). The TIDs associated with the 2011 Tōhoku earthquake have served as a well-documented case demonstrating the phenomenon of earthquake-ionospheric coupling (Chou et al., 2020, 2022; Crowley et al., 2016; Jin et al., 2014; J. Y. Liu et al., 2011; Maruyama & Shinagawa, 2014; Nayak et al., 2022; Rolland, Lognonné, Astafyeva, et al., 2011; Thomas et al., 2022; Tsugawa et al., 2011), with the aid of the observation of dense ground GNSS receivers in Japan. Recently, the occurrence of the 2024 Noto earthquake presents a new opportunity to further investigate the mechanisms behind earthquake-ionospheric coupling.

Studies have identified acoustic waves as a dominant factor in CID (Heki et al., 2022; Inchin et al., 2020; Nina et al., 2020; Sripathi et al., 2020; Srivastava et al., 2021) and have shown that they play a significant role in

Writing – original draft: Bing Zhang, Tong Liu
Writing – review & editing: Tong Liu

understanding the complex interaction between earthquakes, the atmosphere, and the ionosphere. Therefore, the primary focus of this study is to analyze the acoustic wave characteristics and the possible mechanisms associated with this earthquake. Specifically, we will investigate the magnitude of the total electronic content (TEC) disturbance, the wave period, and propagation speed, and particularly discuss their spatial azimuth distribution mechanisms using GNSS-TEC. The following paragraphs will provide a comprehensive examination of these parameters and the expected results.

In terms of the disturbance magnitude of TEC, research has shown that ionospheric disturbances can be caused by earthquakes with a magnitude of at least M_w 6.6 (Cahyadi & Heki, 2015; Perevalova et al., 2014). Additionally, the magnitude of TEC disturbances is nearly proportional to the seismic magnitude (Astafyeva, 2019; Astafyeva et al., 2013). Based on Astafyeva's empirical formula and simulation studies (Martire et al., 2018), it is expected that the 2024 Noto M_w 7.5 earthquake will result in a TEC disturbance magnitude of approximately 0.2–0.3 TECU, while, the second M_w 6.2 event would not case observable disturbances. Such disturbances are typically dominated by acoustic waves, which are ionospheric waves originating from the upper atmosphere and have a period of less than about 15 min. In this process, at first, the atmospheric acoustic waves with a frequency greater than the acoustic cutoff frequency of 3.3 mHz are induced from the epicenter; then, as these waves propagate upward, their frequency decreases below the Väisälä frequency of 2.9 mHz, resulting in their conversion into TIDs in the ionosphere (Astafyeva, 2019; Meng et al., 2019). The waves generated by the main earthquake reach the ionosphere at different times due to variations in their propagation speed. By analyzing both the frequency and speed, it is possible to identify the specific wave responsible for the TID (Maletckii & Astafyeva, 2024). Typically, atmospheric acoustic waves travel at a speed of 1 km/s (Inchin et al., 2020; Srivastava et al., 2021). The recent earthquake in Japan will serve as a test case to validate these patterns.

The direction of ionospheric disturbances' propagation has been discussed in recent years. It can be categorized into two types: annular diffusion and propagation along the north-south direction. The 2011 Tōhoku earthquake in Japan displayed a distinct annular feature (J. Y. Liu et al., 2011; Tsugawa et al., 2011). Moreover, research indicates that earthquake-triggered disturbances can exhibit a two-mode anisotropic propagation pattern, particularly aligned with the north-south direction, as observed in the 2005 Northern California earthquake (Jin, 2018), the 2012 Indian Ocean earthquake (Catherine et al., 2015), the 2015 Nepal earthquake (Reddy & Seemala, 2015), the 2015 Illapel M_w 8.3 earthquake (Meng et al., 2022), and the 28 January 2020 Caribbean/Jamaica earthquake (Chai & Jin, 2021). This phenomenon may be attributed to the fault mechanism and uneven energy release (Chai & Jin, 2021). Numerical simulations have been employed to verify and evaluate this phenomenon (Meng et al., 2022), indicating a relationship between the anisotropic distribution of TID and the source mechanism of earthquakes. The predicted changes in electron density based on Meng's theory generally align with the observed electron density obtained through high-frequency acoustic waves after surface explosions on Earth (Drobzheva & Krasnov, 2003; Y. Huang et al., 2019). The theoretical ionosphere anisotropic electric field in this region has been confirmed through numerical calculations (Huba et al., 2015) and actual observations (C. S. Huang, 2016; Martinis et al., 2011). The phenomenon of CID anisotropic propagation in the 2024 earthquake in Japan may also have a similar mechanism. It remains to be seen whether the CIDs triggered by the 2024 Noto earthquake will exhibit a similar annular distribution to the 2011 earthquake, particularly in terms of its specific azimuthal distribution.

To sum up, this study aims to investigate the characteristics and possible mechanisms of acoustic waves caused by the 1 January 2024, Japanese earthquake with ground TEC observations, including magnitude, period, wave speed, and azimuthal distribution. These findings will provide valuable references for further research to uncover the physical mechanism behind these disturbances.

2. Data and Methods

In this section, data and processing methods are presented.

2.1. Raw Observation Data From Ground-Based GPS Stations and Space Environment Parameters

The data from 1,290 stations of the geographical survey institute established GPS permanent observation station network (GEONET) of Japanese are used. The data is available at https://www.gsi.go.jp/ENGLISH/geonet_english.html and the sampling rate is 30 s.

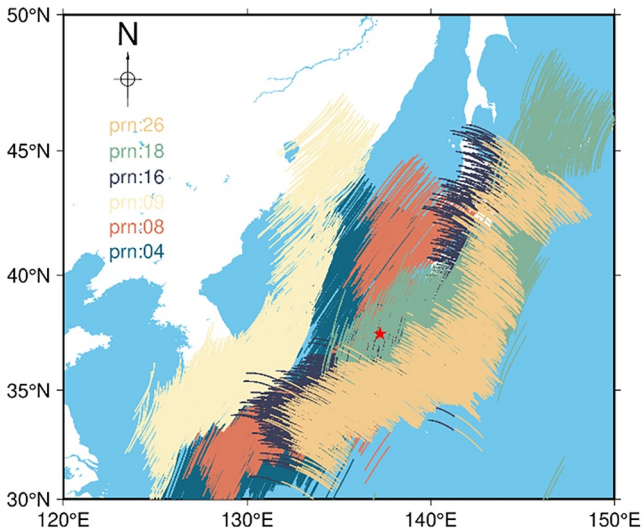

Figure 1. The diagram for the location of the epicenter and ionospheric pierce points.

Multiple solar and geomagnetic indices were queried. The solar radio flux ($f_{10.7}$) index is from https://www.spaceweather.gc.ca/forecast-prevision/solar-solaire/solarflux/sx-5-flux-en.php; The geomagnetic indices (*K*p and Dst) are obtained from https://wdc.kugi.kyoto-u.ac.jp/dst_realtime/index.html and https://kp.gfz-potsdam.de/en/. During the earthquake day, the *D*st index varied from −14 to 9 nT; the $f_{10.7}$ was 136 sfu; and the *K*p index is less than 3. All of the above indices indicate that 1 January 2024 is in a geomagnetically quiet period and that geomagnetically induced changes in the ionosphere will not affect the observation of medium-scale disturbances in the ionosphere at mid-latitudes.

2.2. Acquisition of Time Series Disturbances of TECs

The slant TEC time series of each station-satellite pair was analyzed individually, especially with the data time considered for the period 07:00–08:00 UTC on 1 January 2024. The satellite altitude angle was chosen to be greater than 15°, and the satellite's ionospheric piercing point (IPP) was calculated in a thin shell single-layer model at 250 km altitude, as shown in Figure 1.

The calculation of the ionospheric slant TEC using GNSS can be achieved through code and carrier phase observations. The slant TEC along line-of-sight can be computed with geometry-free (GF) combination (1 TECU = 10^{16} e/m^2) (Ciraolo et al., 2007; T. Liu et al., 2022):

$$\mathrm{TEC} = \frac{1}{40.3} \cdot \frac{f_1^2 f_2^2}{f_1^2 - f_2^2} \cdot (L_1 - L_2 + \mathrm{const} + \varepsilon) \quad (1)$$

where f_1 and f_2 are GNSS carrier frequencies; L_1 and L_2 are carrier phase observations; The constant terms consist of the ambiguity and the Inter-Frequency Bias (IFB). The ambiguity remains constant in the absence of cycle slips, while the IFB can be deemed constant as it changes slowly and has a negligible impact on ionospheric wave observations over a few minutes.

When leveling the GF observation of phase observation L1 and L2 to the GF combination of code, the carrier's cycle slips could potentially introduce false waveforms to the final result. To mitigate this, we detected and repaired the cycle slips using Hatch–Melbourne–Wübbena (Nie et al., 2018) and high-order difference methods (Cai et al., 2013). After that, the satellite frequency bias product is used and the receiver differential code bias is estimated to get the slant TEC.

Actually, the step of leveling carrier phase observations to pseudorange observations isn't strictly necessary. However, for over 1,000 stations, it's still advisable to include this step. This helps in detecting gross errors in the carrier phase data and verifying the quality of the observations, thereby preventing unprocessed gross errors from being misinterpreted as physical phenomena (Tang et al., 2017). In this step, only a constant is subtracted from the carrier phase observations, rather than applying a process like the Hatch filter. This is because the filtering process typically involves smoothing observations over several epochs, which may artificially introduce fluctuations or filter out existing ones, thus compromising the integrity of the true observations (Eisenbeis & Occhipinti, 2021). In fact, for high-quality receivers, simply performing the following fluctuation extraction step on the GF carrier phase observations would suffice (Savastano et al., 2017).

Then, to obtain acoustic waves, the background trend as well as the constant bias in the TEC time series should be removed. Here a combination of Savitzky-Golay filters (J. Chen et al., 2020; Padokhin et al., 2022) and zero-phase fourth-order Butterworth bandpass filter (T. Liu, 2023; T. Liu et al., 2021; Ma et al., 2022) with a pass-band of 2–8.3 mHz is used to get the TEC waves.

Subsequent analysis employs wavelet transforms combined with the *S*-transform (Dash et al., 2003; Ventosa et al., 2008) to resolve wave periods and their temporal evolution. The S-transform is applied to Savitzky-Golay filtered data, leveraging its adaptive time-frequency resolution to enhance detection of complex wave signatures

10.1029/2024SW003957

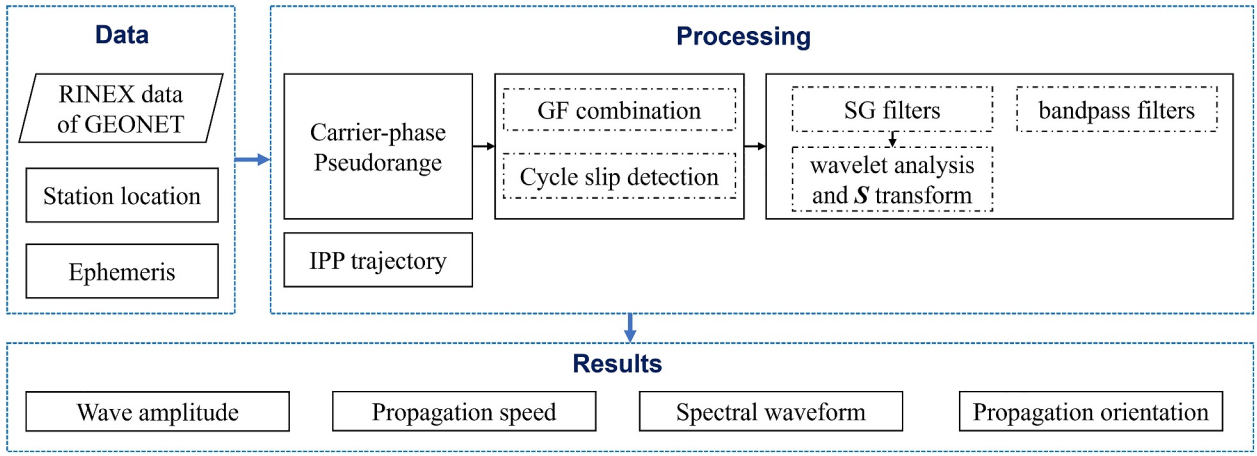

Figure 2. Data processing flowchart: from observations in RNIEX format to ionospheric acoustic waves.

in time series. Finally, the spatial azimuthal distribution of CIDs is mapped through IPP. The full processing workflow is illustrated in Figure 2.

3. Acoustic Wave Features

In this section, we present the case study of acoustic wave features of the 2024 Noto earthquake, including details about the occurrence time, disturbance amplitude, speed, and spectrum features.

3.1. Time of Occurrence and Amplitude of the Dominate Disturbance

As shown in Figure 3, stations 1051, 1046, and 1040 all show significant disturbances. The magnitude of the disturbance is all greater than 0.2 TECU, which is consistent with previous statistical results (Astafyeva et al., 2013) and expectations. The main period of the disturbance occurs from 7:18 to 7:25 UTC. From the timing of its appearance, it is more likely that this disturbance was caused by the first M_w 7.5 earthquake that occurred at 7:10 UTC. This is because it takes roughly 8 min for the atmospheric disturbance to propagate from the epicenter to the ionosphere.

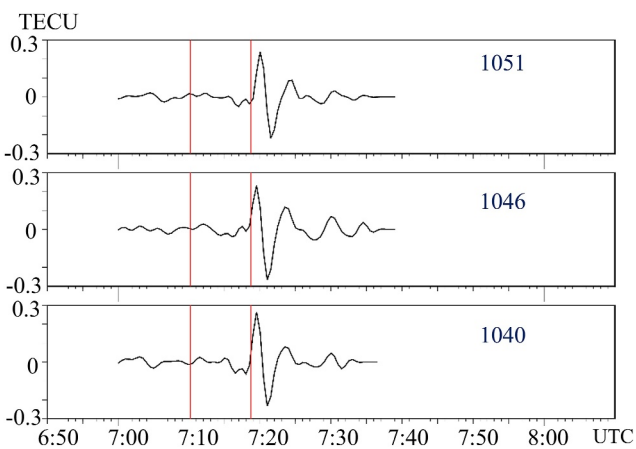

Figure 3. Disturbances observed at stations 1051, 1046, and 1040 of PRN 18. The *x*-axis denotes time; the *y*-axis denotes disturbance magnitude in TECUs; and the two vertical red lines denote the time at which M_w 7.5 and subsequently M_w 6.2 occurred.

The following M_w 6.2 earthquake that occurred at 7:18 may have been associated with the disturbance around 7:30 UTC. However, the magnitude of M_w 6.2 is already below the minimum value of magnitude that can cause ionospheric disturbances (M_w 6.6) (Cahyadi & Heki, 2015). To speculate on whether the disturbance around 07:30 UTC was directly caused by the second earthquake, the tsunami linked to the first earthquake, or other factors, we need to consider the spectral analysis and other content presented in the following subsections.

To ensure that the observed disturbance is not accidental and count all the disturbance magnitude, we have combined all the TEC disturbance sequences at 7:00 and 8:00 UTC on one graph, as shown in Figure 4. The main disturbance period is still between 7:18 and 7:25 UTC, induced by the first M_w 7.5 earthquake. Unlike Figure 3, the TEC disturbance induced by the second M_w 6.2 earthquake almost disappeared around 7:30 UTC. This seems to indicate that the second earthquake did not cause any disturbance. These characteristics of the 0.2 to 0.3 TECU magnitude disturbances induced by the first M_w 7.5 earthquake and the failure of the second M_w 6.2 earthquake to induce this kind of dominate disturbances are consistent with the previous statistical pattern (Astafyeva, 2019; Astafyeva et al., 2013; Cahyadi & Heki, 2015).

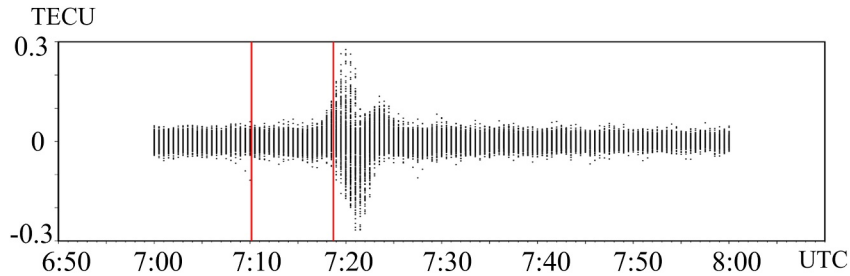

Figure 4. Sequence of total electronic content disturbances for all stations. The *x*-axis denotes UTC, the *y*-axis denotes disturbance magnitude in TECUs; scattered dots denote all observations with a sampling frequency of 30 s; the two red vertical lines denote the time of occurrence of M_w 7.5 and M_w 6.2 in sequence.

3.2. Typical Atmosphere-Ionosphere Acoustic Wave Propagation Velocity Is Detected

Typically, after an earthquake, ionospheric acoustic waves induced by Rayleigh surface waves reach the ionosphere the fastest at 3–4 km/s. Immediately after that, acoustic waves due to crustal motion associated with the seismic source arrive at a speed of 1 km/s. Then after that, gravity waves arrive at about 300 m/s, if at all.

For a better comparison, we have counted some typical cases of atmosphere-ionosphere waves in terms of wave type, time of appearance, propagation speed, and disturbance period (frequency), as shown in Table 1.

By analyzing the speed of propagation of the CID and its appearance time in the ionosphere (i.e., the point where the wave propagation slope intersects the *x*-axis on a time-distance diagram), it becomes possible to determine the type of wave observed during this seismic event. Generally, acoustic waves are typically the main mechanism behind CIDs. Figure 5 illustrates that the dominate wave velocities observed by PRNs 4, 8, 9, 16, 18, and 26 are approximately 1 km/s, which is characteristic of acoustic waves. Its slope intersects the *x*-axis at approximately 7:18 UTC, precisely 8 min after the earthquake, which aligns with the appearance time of acoustic waves observed after previous earthquakes (Chai & Jin, 2021; Haralambous et al., 2023; Inchin et al., 2020; Maletckii et al., 2023). Subplots (a) and (e) display elevated speeds (approximately 3–4 km/s), which align with Rayleigh surface waves. Notably, panel (a) clearly shows the trajectories of two types of waves with speeds of 1 km/s and 3–4 km/s. These Rayleigh surface waves produce higher-frequency acoustic waves through upward coupling and propagate more rapidly than direct acoustic waves.

Figure 5 displays at least 1.5 cycles of the ionospheric disturbance. PRNs 16 and 26 show 1.5 cycles with an additional sub-obvious cycle at ~7:30 UTC. The wave speeds here are slightly lower than earlier acoustic waves (~1 km/s), likely due to two factors: (a) resonance effects modulating post-earthquake disturbances (Chou et al., 2020; Rolland, Lognonné, Astafyeva, et al., 2011; Tsugawa et al., 2011) and (b) tsunami-induced acoustic gravity waves from the coastal earthquake, which propagate slower and exhibit longer periods than CIDs (Ghent & Crowell, 2022; Putra et al., 2023; Yang et al., 2022).

Table 1
Statistics on the Characteristics of Ionospheric Waves Induced by Rayleigh Surface Wave, Acoustic Waves, and Acoustic Gravity Waves After Earthquakes

Type	Cases	Year and location	Time delay since the earthquake (min)	Speed (km/s)	Frequency
Rayleigh surface wave	Jin et al. (2017)	2012 Haida Gwaii	10	2.2	4.2 mHz
Rayleigh surface wave	Jin (2018)	2005 offshore California	10	1.5–2.3	5.2 mHz
Rayleigh surface wave	Heki et al. (2022)	2010 Maule	10	4	
Rayleigh surface wave	Rolland, Lognonné, and Munekane (2011)	2003 Shushengchong	10	3.5	5 Hz
		2008 Wenchuan			
Acoustic wave	Cahyadi et al. (2022)	2016 West Sumatra	10	1–1.7	4 mHz
		2018 Baru		1–1.1	
Acoustic wave	Srivastava et al. (2021)	2012 Sumatra	10	1–1.1	4.4 mHz
Gravity wave			30	0.21	1 mHz
Gravity wave	Heki et al. (2022)	2010 Maule	30	0.25	

10.1029/2024SW003957

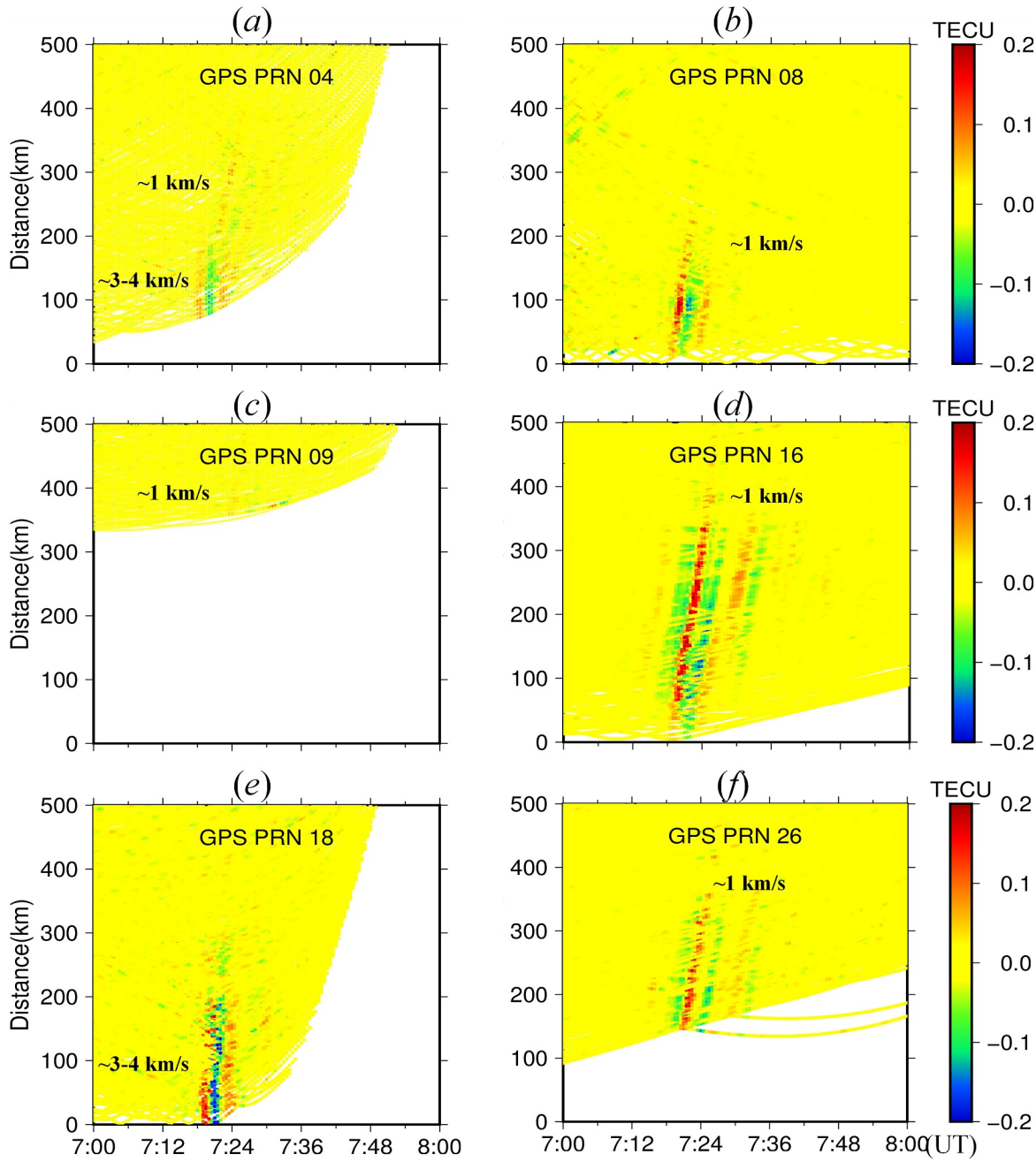

Figure 5. Time-distance diagram of CID propagation. From subplot (a) to (f), the GPS satellites 4, 8, 9, 16, 18, and 26 are shown in order; the horizontal coordinates denote seven to eight o'clock (UTC); the vertical coordinates denote the distance from the ionospheric piercing point to the epicenter in kilometers; and the color-bar denotes the magnitude of the total electronic content disturbance.

3.3. Spectral Analysis of the Detected Acoustic Waves

Figure 6 presents the time series of ionospheric disturbance of GPS PRN 16 received by stations 0624, 0625, 3095, and P115, along with their corresponding time-frequency maps generated through wavelet analysis. The upper part of each subplot represents the ionospheric disturbance, while the lower part displays the time-frequency analysis results obtained through wavelet analysis. The time-frequency map demonstrates the correspondence between the time sequence disturbance and the spectrum.

10.1029/2024SW003957

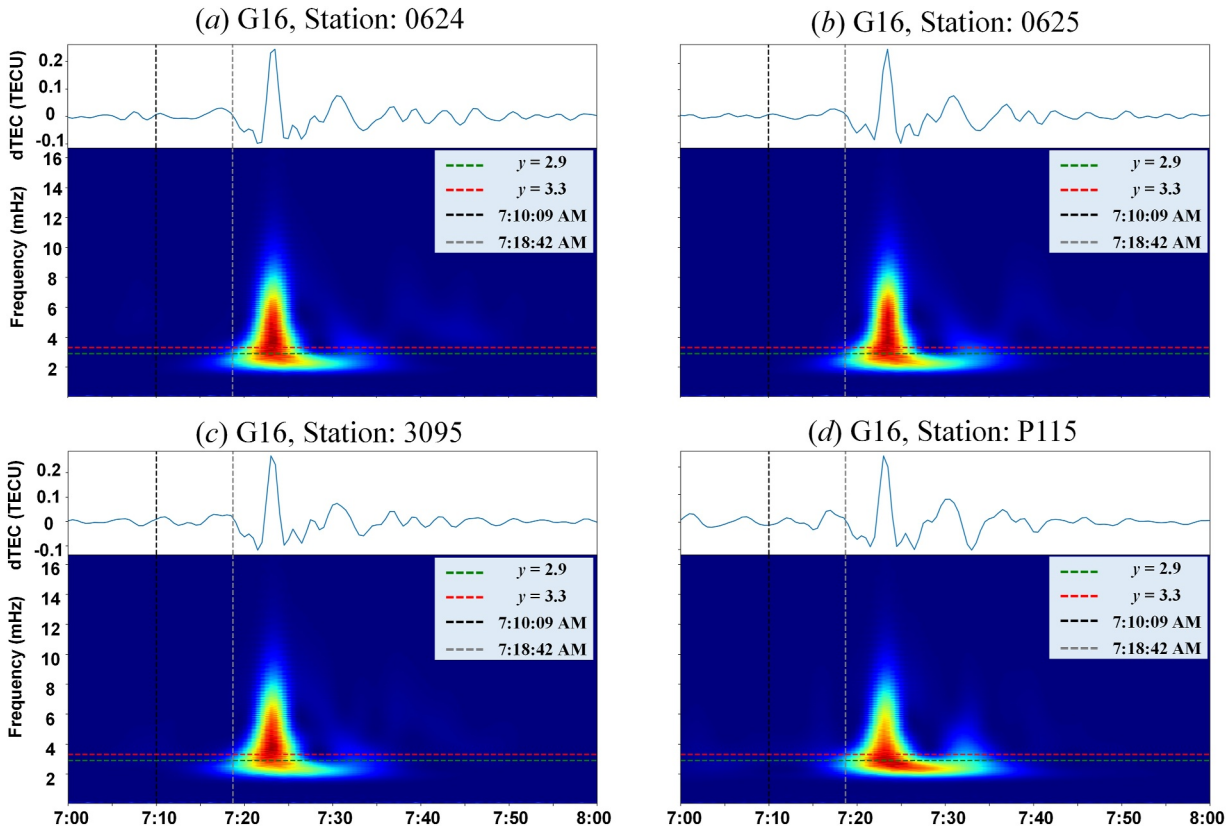

Figure 6. Spectral analysis of acoustic waves. The *x*-axis represents Universal Time; the *y*-axis represents the frequency and magnitude of the disturbance; the brightness represents the intensity of the spectrum; the four subplots represent stations 0624, 0625, 3095, and P115, respectively; the black and gray vertical lines indicate the occurrence times of the first 7.5 M_w and the subsequent 6.2 M_w, respectively; the red and green horizontal lines represent the Brunt-Vaisala frequency (3.3 mHz) and the acoustic cut-off frequency (2.9 mHz), respectively.

Besides the clear wave seen at 7:24 UTC, Figure 6 also shows a faint acoustic resonance signal occurring around 7:30 UTC, with a wave cycle of roughly 10 min. The faint acoustic resonance signal observed around 07:30 UTC (Figure 6d) is more plausibly attributed to the M_w 6.2 aftershock than to tsunami activity from the mainshock. This interpretation is supported by multi-faceted evidence: The disturbance exhibits characteristic acoustic wave signatures with a 10-min period and phase velocity of ∼1.2 km/s, distinct from tsunami-generated gravity waves that typically propagate below 0.5 km/s (Alfonsi et al., 2024; Heki et al., 2022; Yang et al., 2022). Critically, it is demonstrated that the Noto earthquake's tsunami originated primarily from submarine landslides rather than direct fault displacement (Yanagisawa et al., 2024). In a such scenario, gravity waves or ionospheric disturbances due to gravity waves are not observed in the ionosphere. This source mechanism explains the absence of tsunami-linked TEC disturbances in our observations. Furthermore, the 07:30 UTC disturbance emerged merely 6 min after the aftershock, aligning with acoustic wave vertical propagation timescales but physically inconsistent with tsunami-ionosphere coupling, which requires ≥30 min for gravity wave energy transfer (Ghent & Crowell, 2022; Heki et al., 2022). The combined evidence from wave mode characteristics, tsunami generation mechanisms, and propagation timing conclusively favors an aftershock origin for this ionospheric wave.

3.4. Snapshots of the Acoustic Waves Travel South

The sequential snapshots in Figures 7 and 8 reveal the evolution of CIDs dominated by AGWs, with predominant equatorward propagation aligned with the geomagnetic field vectors (black arrows in Figures 7 and 8). Earth magnetic field are calculated using International Geomagnetic Reference Field (Alken et al., 2021). The disturbance evolution exhibits four phases:

1. Initial excitation phase (07:18 UTC):
   The primary disturbance emerged at 37.50°N, 137.24°E (Figure 7a), displaying localized TEC enhancement.

10.1029/2024SW003957

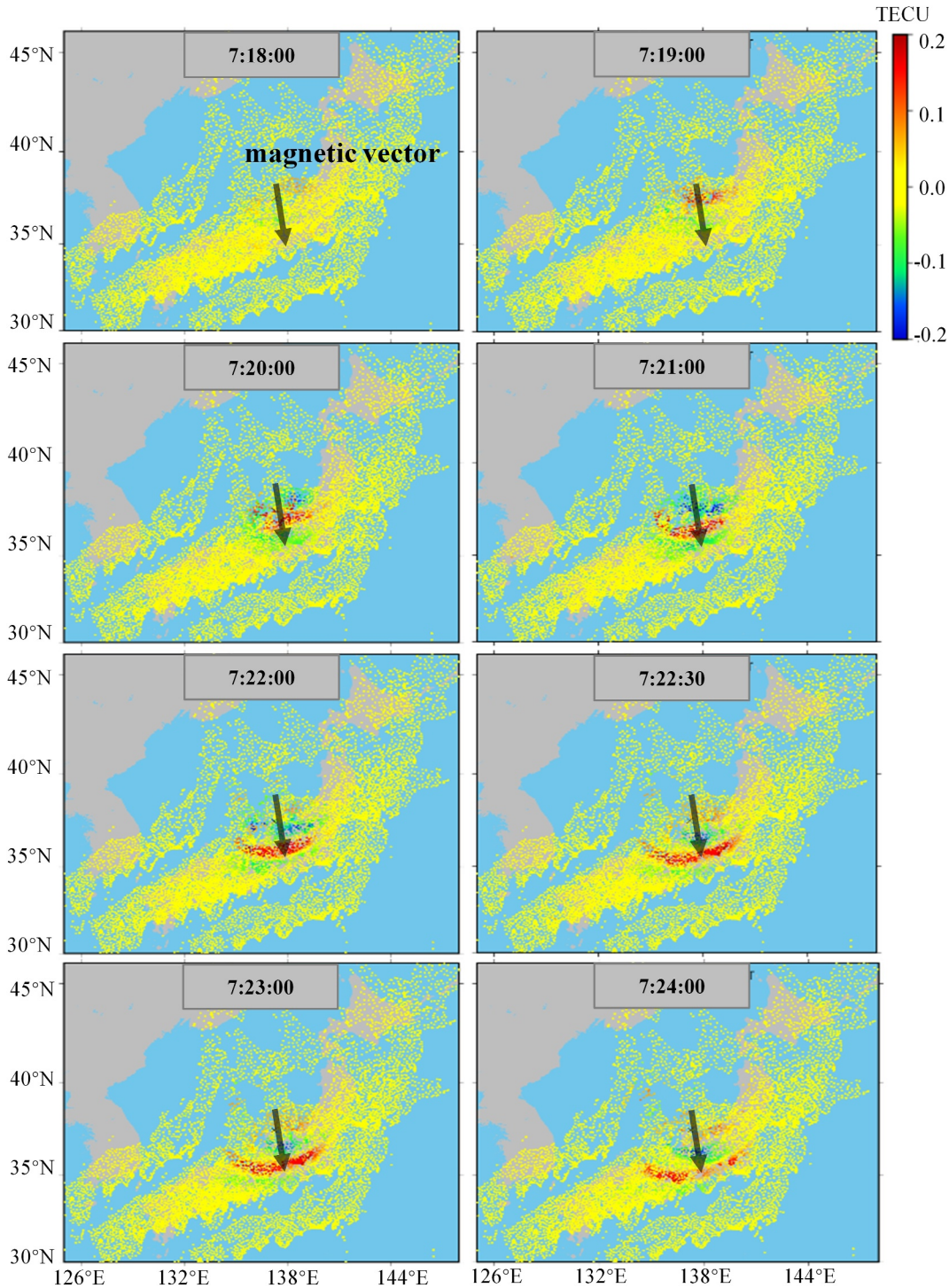

Figure 7. Spatial propagation map of CID from 7:18 to 7:24 UTC. The *x*-axis and *y*-axis represent longitude and latitude, respectively. All the scatter points represent IPPs. Each subplot represents a different moment with a one-minute interval. The color axis represents the magnitude of the disturbance in TECU units. The black arrow indicates the direction of the local magnetic field: angle with geographic north (magnetic declination): 8.7°.

10.1029/2024SW003957

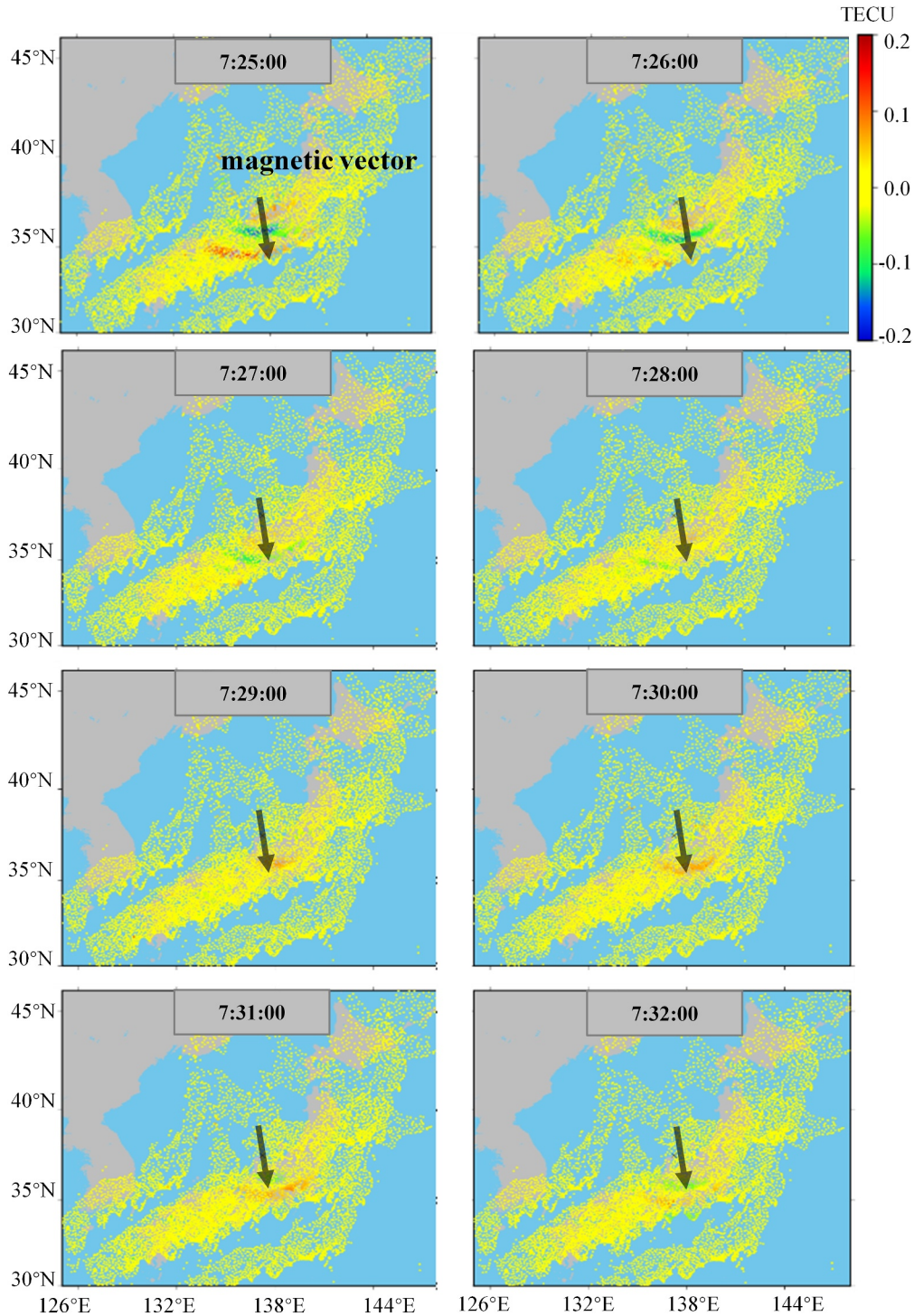

Figure 8. Spatial propagation map of CID from 7:25 to 7:32 UTC. The *x*-axis and *y*-axis represent longitude and latitude, respectively. All the scatter points represent IPPs. Each subplot represents a different moment with a one-minute interval. The color axis represents the magnitude of the disturbance in TECU units. The black arrow indicates the direction of the local magnetic field: angle with geographic north (magnetic declination): 8.7°.

The alignment between the initial propagation azimuth (≈180° ± 15°) and the local geomagnetic field orientation (inclination angle 51.9°, declination 8.7°) suggests magnetic field guidance of wave energy transfer, consistent with previous findings on CID channeling along magnetic field lines (Heki & Ping, 2005; Rolland et al., 2013).

2. Anisotropic expansion phase (07:19–07:20 UTC):
   The disturbances propagated preferentially southward along the geomagnetic meridian, while showing limited westward/eastward expansion. This directional preference correlates with (a) the magnetic zenith effect enhancing AGW detection along field-aligned directions (Bagiya et al., 2019), and (b) background ionospheric gradients facilitating plasma transport in the magnetic southward direction.
3. Wavefront maturation phase (07:21–07:23 UTC):
   Well-defined wavefronts developed with phase velocities of about 1 km/s, characteristic of acoustic-gravity wave modes. The persistent southward propagation demonstrates stronger coupling efficiency along the magnetic field-aligned direction compared to perpendicular paths, as predicted by magneto-ionospheric coupling theory (Kundu & Bagiya, 2024).
4. Energy dissipation phase (07:23–07:24 UTC):
   Disturbance intensity attenuated significantly below 35°N, likely due to collisional damping increasing at lower altitudes and geometric spreading loss during field-guided propagation.
   Notably, the CID propagation direction (≈182° ± 15°) shows well alignment with the geomagnetic field orientation (declination 8.7°), indicating magnetic channeling dominates over seismic source directivity in governing wave propagation. This observation aligns with multi-event analyses demonstrating persistent equatorward CID propagation regardless of faulting mechanisms (Kundu & Bagiya, 2024). The secondary disturbance near 35°N 138°E after 07:26 UTC likely originated from the M_w 6.2 aftershock, exhibiting similar magnetic field-aligned propagation characteristics.

3.5. Ionosonde Observations Near the Epicenter

Ionosonde data from Kokubunji Station (east of the Noto Peninsula epicenter) recorded sporadic 1–3 MHz echoes at ∼150 km altitude between 07:00 and 07:25 UTC (16:00–16:25 Japan Standard Time, JST) on 1 January 2023, as shown in Figure 9. These signals were unrelated to the M_w 7.5 earthquake that occurred at 7:10, as they appeared 10 min before the mainshock.

At 16:10 JST (sunset in Noto: ∼16:45 JST in early January), the sun's elevation angle was approximately 12° (solar zenith angle $\chi \approx 78°$), placing it low on the southwestern horizon. This timing corresponds to pre-sunset ionospheric recombination, where decreasing solar radiation triggers electron density decay in the F-layer (Afraimovich, 2008). The observed descending ionospheric layer aligns with typical dusk-related dynamics, distinct from co-seismic disturbances that arise after earthquake-generated acoustic waves reach the ionosphere (∼10–20 min post-mainshock).

Contrastingly, Yamagawa station southwest of the epicenter recorded unique sporadic-E layers from 7:15 to 7:35 UTC (2 MHz, 200 km altitude), marked by altitude oscillations correlating with seismic wave arrival times. This perturbation pattern diverges from conventional CIDs that typically manifest as wave-like electron density fluctuations. The observed sporadic-E layers may stem from AGWs generated by crustal deformation (Gao et al., 2023), which propagate vertically and modify ionospheric plasma through neutral-atmosphere coupling. Concurrent electromagnetic disturbances from fault zone charge redistribution (H. Chen et al., 2022) and earthquake-induced atmospheric compositional changes (J. Liu et al., 2023) could further amplify these effects through altered E-region dynamo processes.

Notably, these sporadic-E features showed strict spatial localization, appearing only at Yamagawa station along the southern seismic wavefront while remaining absent at northeastern (Wakkanai) and distant southwestern (Okinawa) stations. This directional specificity aligns with GPS-TEC observations of southward-propagating disturbances and excludes non-seismic sources like large-scale TIDs. The absence of similar signatures in South Korean ionosonde data west of the epicenter further confirms the anisotropic radiation pattern of seismic ionospheric effects.

Although sporadic-E layer formation following earthquakes remains less common than typical CIDs (Tachema et al., 2024), the multi-mechanism framework proposed here—encompassing AGW forcing, electromagnetic coupling, and atmospheric chemistry alterations—provides a consistent explanation for their occasional

10.1029/2024SW003957

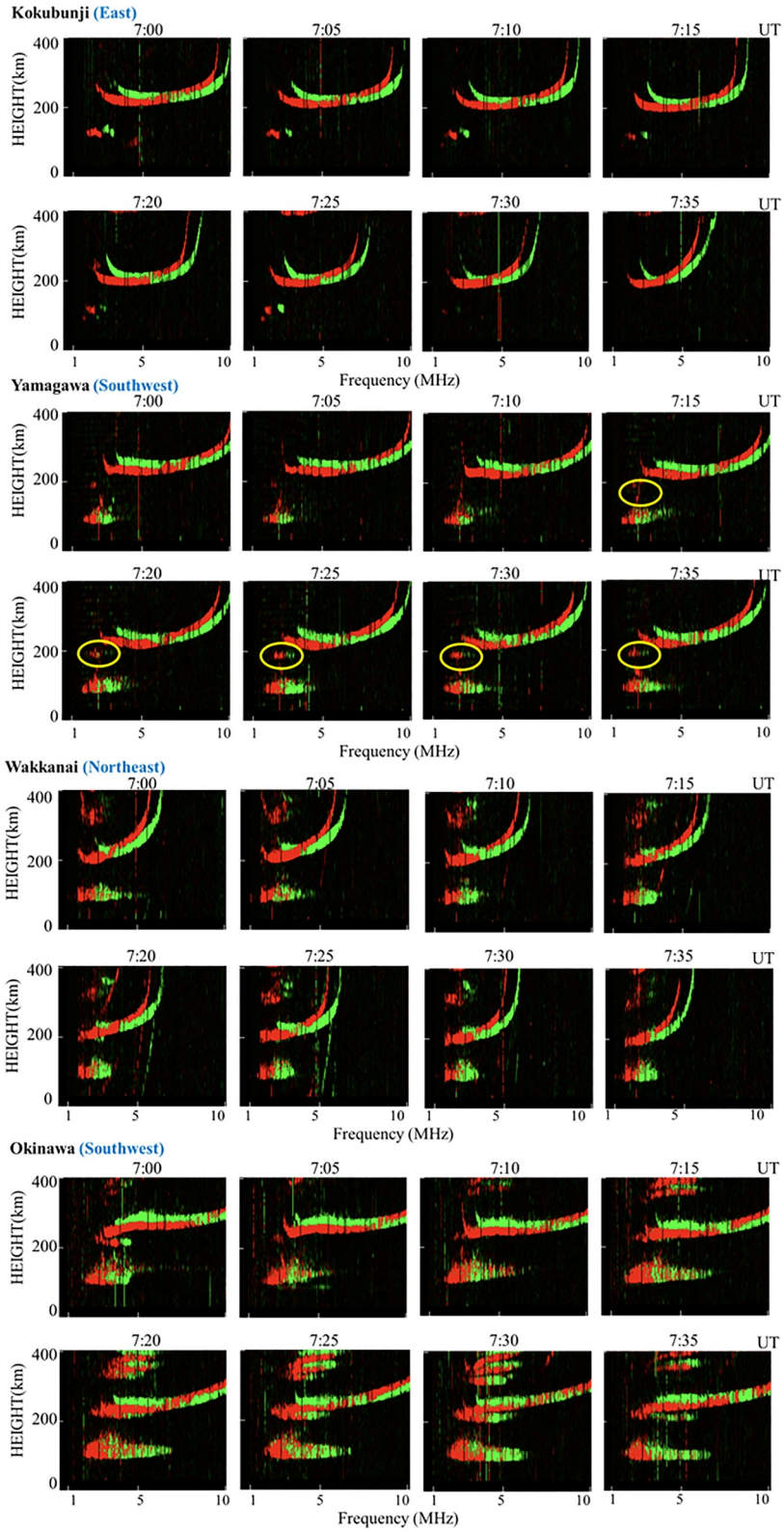

Figure 9.

occurrence. Crucially, spectral analysis confirmed minimal interference from background ionospheric variability, with earthquake-related features exhibiting higher frequency content (1.2–2.5 mHz) compared to solar terminator effects (<0.8 mHz). These findings collectively demonstrate the viability of using directional ionosonde anomalies as complementary indicators of seismic ionospheric perturbations.

4. Mechanism Analysis and Discussion

This section shows an analysis of factors affecting the southward propagation of the coseismic ionospheric acoustic waves.

At the source of an earthquake, acoustic waves are likely to propagate uniformly in all directions. However, during their propagation, both their amplitude and period undergo changes. On the one hand, as the wave ascends into regions of lower atmospheric density, the amplitude of the wave increases in accordance with the conservation of energy principle (Hines, 1972, 1974). Simultaneously, the energy loss due to friction between the wave and air molecules during propagation results in a decrease in amplitude (Blanc, 1985; Y. Huang et al., 2019). Consequently, some disturbances with inadequate energy fail to propagate into the ionosphere. The waves that reach the ionosphere typically possess a high initial velocity and energy.

Even when the wave's energy is sufficient to propagate to the ionosphere, the observed TID is a result of its possible interaction and coupling with geomagnetic field, land displacement, magnetic and wind fields (Y. Huang et al., 2019; Vadas, 2007). In this case, the anisotropic CID propagation (mean azimuth 182° ± 15°) aligns more closely with the local geomagnetic field orientation (declination 8.7°; Figure 7) than with the vertical displacement vectors, demonstrating magnetic channeling as the primary driver. Next, we delve into the detailed coupling effects.

4.1. Coupling With the Geomagnetic Field

For the waves propagated successfully into the ionosphere, due to the interaction with the geomagnetic field, the atmospheric waves lose their isotropic characteristics and become anisotropic and propagate as shown in Equation 2 (Drobzheva & Krasnov, 2003; Y. Huang et al., 2019; Krasnov et al., 1991).

$$\frac{\partial N}{\partial t} = -\left[N_0\left(\frac{v}{L}\sin^2\Theta\right) + v\frac{\partial N_0}{\partial z}\cos\varphi\cos\Theta\right] \tag{2}$$

where ∂N donates the changes in electron density due to acoustic waves; N_0 is the background ionospheric electronic density; v is the velocity of the neutral particle oscillating by acoustic wave; L is the scale length; the term "v/L" is the frequency (inverse of time); z is altitude; Θ is the angle between the magnetic field line and the acoustic vector; φ is the angle between the magnetic field line and the up direction.

Previous studies have established that CID anisotropic propagation is primarily governed by the local geomagnetic field geometry (Huba et al., 2015; Nickolaenko & Hayakawa, 2014), exhibiting preferential equatorward propagation along magnetic field lines rather than simple geographic north-south directions. This directional control arises from two synergistic effects: (a) Ion-Neutral Collisional Constraint: When ion gyrofrequency dominates over collision frequency and wave frequency (ω), plasma motions become strictly field-aligned (Huba et al., 2015); (b) Magnetic Zenith Amplification: AGWs propagating along magnetic field lines experience enhanced detectability due to prolonged ionospheric traversal and reduced cross-field diffusion (Bagiya et al., 2019; Rolland et al., 2013).

Consequently, momentum transfer through ion-neutral collisions generates TIDs propagating preferentially along magnetic field lines (Y. Huang et al., 2019). Our observations confirm this mechanism: CID propagation azimuth (about 180° ± 15°) aligns with local magnetic declination (8.7°), demonstrating magnetic guidance over source

Figure 9. The Ionosonde observations in Japan of four stations: Kokubunji, situated to the east of the epicenter; Yamagawa, located to the southwest of the epicenter; Wakkanai, positioned to the northeast of the epicenter; and Okinawa, also situated to the southwest of the epicenter. Each station's data is presented in eight subplots, each representing an ionogram for the 7:00–7:35 UTC, with intervals of 5 min between them. The horizontal axis denotes frequency, while the vertical axis indicates the height of the ionosphere. Included annotations distinguishing O-mode (red traces) and X-mode (green traces) reflections, which arise from the magneto-ionic splitting effect.

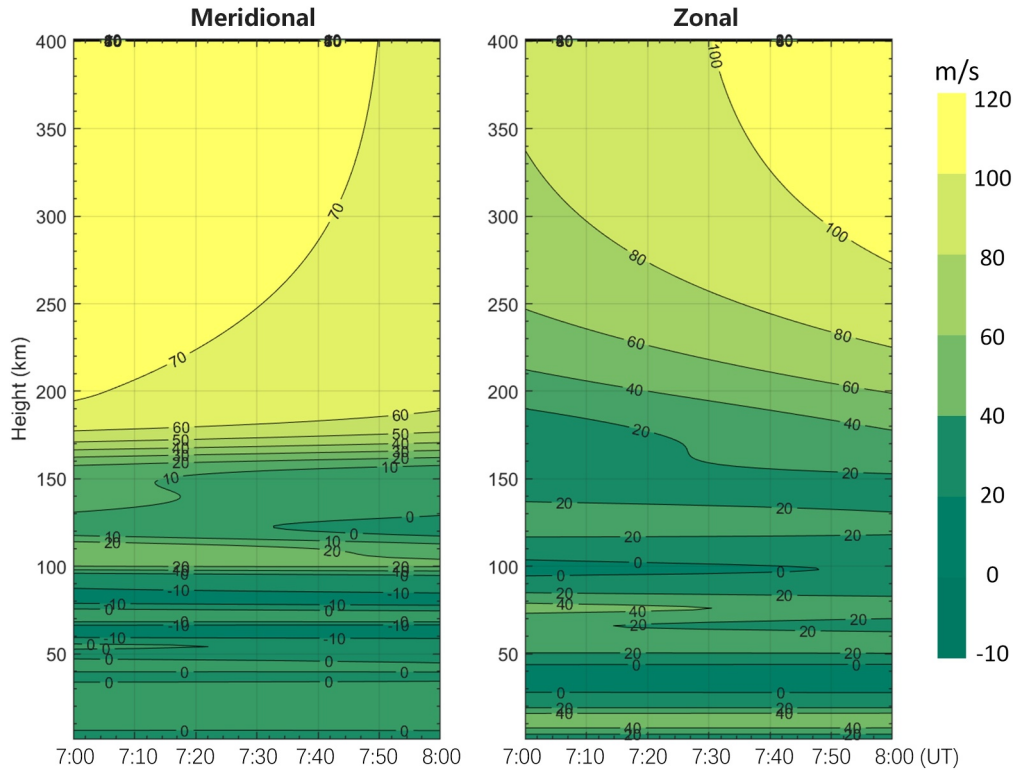

Figure 10. The wind field diagrams above the seismic source with the HWM14 (Horizontal Wind Model 14) model. The left subplot represents the Meridional (north-south) direction, while the right subplot depicts the Zonal (east-west) direction. In these diagrams, the eastward and northward directions are considered positive; Contour lines are marked in m/s. The horizontal axis represents time, spanning from 7:00 to 8:00 UTC, and the vertical axis indicates altitude, ranging from 0 to 400 km.

directivity. Equation 2 explicitly links electron density variations to magnetic field geometry through the Θ angle. Specifically, the cosΘ term maximizes when AGWs propagate parallel to B, explaining the observed equatorward CID intensification. This angular dependence has been validated across diverse tectonic settings (Kundu & Bagiya, 2024).

4.2. The Wind-Filtering Effect

In the case of the 2024 Noto earthquake, only southward-propagating CIDs were detected. One plausible explanation is that acoustic waves spread outward in a circular pattern (Y. Huang et al., 2019) from the initial triggering and, due to the local wind field, the northward propagating acoustic waves were either hindered or transformed into horizontally oriented gravity waves (Vadas, 2007; Vadas et al., 2018). That is, the coupling between the background wind and acoustic waves can result in a filtering effect (Cowling et al., 1971). Recent studies have revealed that as atmospheric waves propagate upwards, their chances of successfully reaching the ionosphere increase when they propagate against the wind direction (Lay et al., 2015, 2018; Medvedev et al., 2017; Nie et al., 2024; Oinats et al., 2016). Conversely, when waves propagate with the wind, they tend to maintain their horizontal wave speeds and struggle to propagate vertically. To gain a more profound understanding of this coupling effect of the wind field on TIDs, we have plotted the wind field model (Drob et al., 2015) above the seismic source in Figure 10.

In the meridional subplot of Figure 10, the wind field between 1 and 150 km remains mostly at or close to 0 m/s at various altitudes, fluctuating within a range of ±10 m/s from north to south. However, from 150 to 200 km, the northward-propagating wind velocity experiences a sharp increase from 10 m/s to 70 m/s. This critical altitude marks the primary region where atmospheric waves propagate upwards and couple with the ionosphere (Astafyeva, 2019; Lay et al., 2018). Waves that propagate against the wind tend to retain their upward components more readily, manifesting as ionospheric waves. The steep increase in northward wind velocity between 150 and

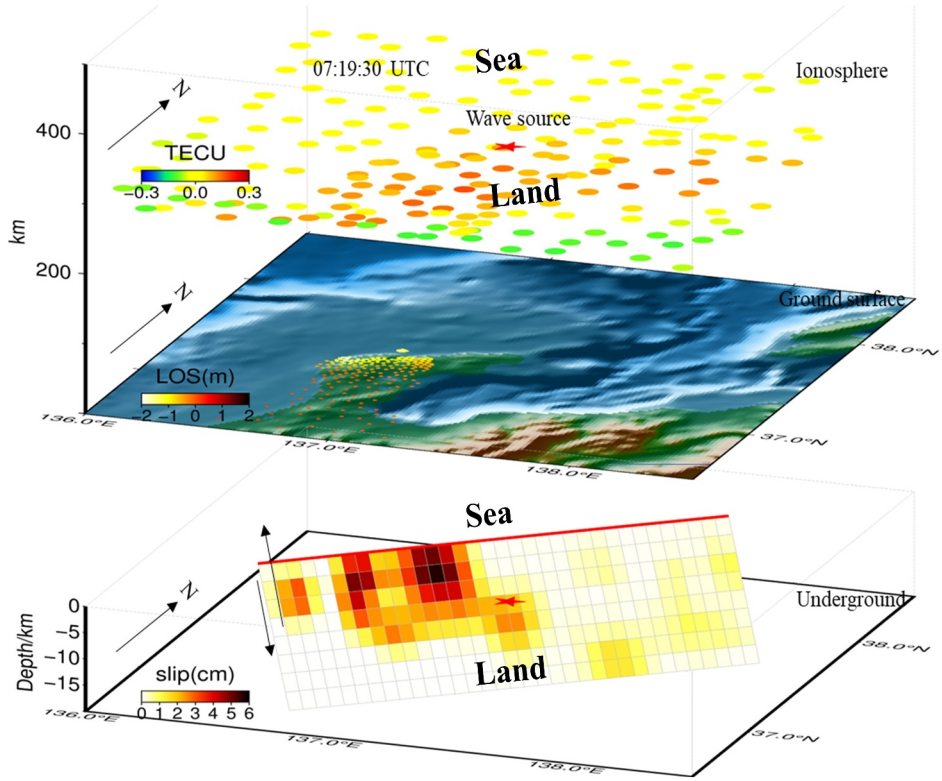

Figure 11. The figure displays, from top to bottom, the near-field ionospheric disturbance distribution, surface deformation, and subsurface co-seismic slip distribution. In the top panel, disturbances at 07:19:30 UTC are shown, with dark red and blue-green dots indicating areas of significant ionospheric disturbance, while yellow dots represent regions with no detected disturbance. The wave source is marked with a star symbol. The middle panel shows surface deformation, with noticeable deformation points concentrated around and south of the epicenter. The bottom panel illustrates the co-seismic slip, highlighting substantial subsurface displacements—up to 6 cm—within approximately 1 degree of latitude and longitude around the epicenter on land.

200 km likely plays a significant role in why only southward-propagating ionospheric waves are predominantly observed, rather than in the directions of both north and south.

In essence, the directional movement of TIDs triggered by atmospheric waves is susceptible to the interplay of the local wind field and geomagnetic environment. Specifically, in the context of the Noto earthquake, it is reasonable to assume that the northward-moving waves encountered resistance from the prevailing downwind conditions. As a result, only the residual disturbance managed to ascend into the ionosphere, where it interacted with the magnetic field lines aligned in the north-south direction. This interaction ultimately gave rise to the observed southward propagation pattern of the TID.

4.3. Rupture and Crustal Motion Effects

As shown in Figure 11, the vertical sequence illustrates 3 subplots of the Noto earthquake: near-field ionospheric disturbance distribution at the top, surface deformation in the middle, and co-seismic slip distribution at the bottom. The crustal slip distribution, represented by a colored grid, was estimated post-earthquake by the United States Geological Survey (USGS) using a single rectangular fault model. Surface deformation, depicted with colored dots, derives from JAXA's ALOS-2/PALSAR-2 descending interferometric data spanning two epochs (2023-12-06 and 2024-01-03), with data processing methods detailed in reference (Zhang et al., 2024). Combined with the thrust-fault focal mechanism, these observations indicate coseismic vertical displacements approaching 2 m near the epicenter.

The Noto epicenter is bounded by oceanic regions to the north and continental land to the south. The contrasting mechanical properties of land and ocean surfaces may introduce differences in the efficiency of seismic

deformation coupling with the atmosphere. Previous studies indicate that continental crust, with its higher rigidity, could experience faster and potentially larger coseismic deformation than oceanic regions (Rolland, Lognonné, Astafyeva, et al., 2011; Rolland, Lognonné, & Munekane, 2011). Such differences might imply that vertical displacements over land, given an equivalent seismic source, may couple more rapidly with the atmosphere, possibly generating stronger upward-propagating acoustic waves.

As illustrated in Figure 11, CIDs are absent over the northern oceanic area but detected over the southern continental region. The initial CID arrival in the ionosphere (07:19:30 UTC) appears consistent with the idea that rapid, large-amplitude crustal deformation over land could enhance atmospheric acoustic wave excitation compared to oceanic crust. This spatial pattern aligns broadly with theoretical models suggesting that land's structural properties might amplify ionospheric responses to seismic energy transfer, though other contributing factors cannot be ruled out.

4.4. Detection of Ionospheric Disturbances From the M_w 6.2 Aftershock

The detection of CIDs triggered by the M_w 6.2 aftershock (07:26 UTC) advances our understanding of ionospheric responses to moderate-magnitude seismic events. Conventional studies suggest M_w 6.6 as the lower threshold for CID generation (Cahyadi & Heki, 2015), yet our findings align with recent evidence showing that shallow, optimally oriented earthquakes as small as M_w 5.6 can produce detectable ionospheric perturbations under favorable conditions (Maletckii et al., 2023; Sanchez et al., 2022).

The aftershock-induced CID exhibits three distinct observational features. First, an acoustic wave signature appears as a about 5-min periodic disturbance emerging at 07:30 UTC, propagating equatorward at ∼1 km/s. This phase velocity matches the theoretical range of acoustic-gravity waves at 1.0–1.8 km/s (Heki, 2024), distinguishing it from slower tsunami-generated gravity waves (<0.5 km/s). Second, the disturbance originates at 35.12°N, 138.04°E—within 15 km of the aftershock epicenter—and propagates along the geomagnetic meridian (with azimuth angle about 170° ± 20°), mirroring the magnetic guidance mechanism observed in the mainshock. Third, the signal onset at 07:26:30 UTC corresponds to the seismic P-wave arrival time (07:24:50 UTC) plus a 100-s atmospheric acoustic travel time to the F2-layer (300 km altitude).

The detectability of this sub-threshold CID likely results from synergistic geophysical factors. The aftershock's shallow hypocenter (10 km depth) and steep fault dip angle (USGS finite model) enhanced vertical ground velocities to 0.8 m/s, 2.5 times higher than typical M_w 6.2 events (Astafyeva, 2019). Concurrently, elevated background total electron content (25 TECU) and quiet geomagnetic conditions ($K_p = 2$) minimized plasma diffusion losses, amplifying weak disturbances (Sanchez et al., 2022). Additionally, equatorward propagation along the geomagnetic field lines extended the CID detection range to 500 km, counteracting geometric spreading attenuation that typically obscures isotropic signals (Maletckii & Astafyeva, 2024).

5. Conclusions

The 2024 M_w 7.5 Noto Peninsula earthquake provided critical insights into seismic-ionospheric coupling mechanisms through dense GNSS observations. Key findings include:

CIDs propagated exclusively southward at ∼1 km/s, aligned with the local geomagnetic field declination (8.7°). This anisotropy underscores magnetic guidance as the primary driver, facilitated by ion-neutral collisional constraints and field-aligned plasma transport. The M_w 6.2 aftershock generated detectable CIDs (∼1 km/s, 10-min period), challenging the conventional M_w 6.6 detection threshold. Enhanced vertical ground velocities, elevated background TEC, and geomagnetic quietness may enable this observation, highlighting the role of optimal source and ionospheric conditions. Northward thermospheric winds (70 m/s at 200 km altitude) suppressed northward CID propagation, while land-ocean coupling differences amplified vertical displacements over continental regions. These factors, combined with magnetic channeling, explain the observed southward preference.

The study corroborates theoretical models of acoustic wave propagation while revealing site-specific interactions between seismic forcing and geophysical filters. The detection of moderate-magnitude CIDs demonstrates the potential for expanding ionospheric monitoring to smaller earthquakes under favorable conditions, advancing space weather applications and multi-scale seismic hazard assessment.

Data Availability Statement

The data from 1,290 stations of the geographical survey institute established GPS permanent observation station network (GEONET) of Japanese are used. The download website is https://www.gsi.go.jp/ENGLISH/geonet_english.html. *The dst* index is from https://wdc.kugi.kyoto-u.ac.jp/dst_realtime/index.html; *F*10.7 index is from https://www.spaceweather.gc.ca/forecast-prevision/solar-solaire/solarflux/sx-5-flux-en.php; *K*p index is from https://kp.gfz-potsdam.de/en/. The ionosonde data of Japan is from https://wdc.nict.go.jp/Ionosphere/en/. The ionosonde data of Korea is from https://spaceweather.kasa.go.kr/eng/obsenv1.do. The data of United States Geological Survey (USGS) is from https://www.usgs.gov/products/data.

Acknowledgments
This study was supported by the National Key R&D Program of China (2022YFC3003800). We are grateful for the open-access HWM wind field model. Some figures were prepared using the public domain Generic Mapping Tools (GMT).

References

Afraimovich, E. (2008). First GPS-TEC evidence for the wave structure excited by the solar terminator. *Earth, Planets and Space*, *60*(8), 895–900. https://doi.org/10.1186/bf03352843

Alfonsi, L., Cesaroni, C., Hernandez-Pajares, M., Astafyeva, E., Bufféral, S., Elias, P., et al. (2024). Ionospheric response to the 2020 Samos earthquake and tsunami. *Earth, Planets and Space*, *76*(1), 1–14. https://doi.org/10.1186/s40623-023-01940-2

Alken, P., Thébault, E., Beggan, C. D., Amit, H., Aubert, J., Baerenzung, J., et al. (2021). International geomagnetic reference field: The thirteenth generation. *Earth, Planets and Space*, *73*, 1–25.

Artru, J., Ducic, V., Kanamori, H., Lognonné, P., & Murakami, M. (2005). Ionospheric detection of gravity waves induced by tsunamis. *Geophysical Journal International*, *160*(3), 840–848. https://doi.org/10.1111/j.1365-246x.2005.02552.x

Astafyeva, E. (2019). Ionospheric detection of natural hazards. *Reviews of Geophysics*, *57*(4), 1265–1288. https://doi.org/10.1029/2019rg000668

Astafyeva, E., Shalimov, S., Olshanskaya, E., & Lognonné, P. (2013). Ionospheric response to earthquakes of different magnitudes: Larger quakes perturb the ionosphere stronger and longer. *Geophysical Research Letters*, *40*(9), 1675–1681. https://doi.org/10.1002/grl.50398

Bagiya, M. S., Sunil, A., Rolland, L., Nayak, S., Ponraj, M., Thomas, D., & Ramesh, D. S. (2019). Mapping the impact of non-tectonic forcing mechanisms on GNSS measured coseismic ionospheric perturbations. *Scientific Reports*, *9*(1), 18640. https://doi.org/10.1038/s41598-019-54354-0

Blanc, E. (1985). Observations in the upper atmosphere of infrasonic waves from natural or artificial sources-A summary. *Annales Geophysicae*, *3*, 673–687.

Cahyadi, N., & Heki, K. (2015). Coseismic ionospheric disturbance of the large strike-slip earthquakes in North Sumatra in 2012: M w dependence of the disturbance amplitudes. *Geophysical Journal International*, *200*(1), 116–129. https://doi.org/10.1093/gji/ggu343

Cahyadi, N., Muslim, B., Pratomo, G., Anjasmara, M., Arisa, D., Rahayu, R. W., et al. (2022). Co-seismic ionospheric disturbances following the 2016 West Sumatra and 2018 Palu earthquakes from GPS and GLONASS measurements. *Remote Sensing*, *14*(2), 401. https://doi.org/10.3390/rs14020401

Cai, C., Liu, Z., Xia, P., & Dai, W. (2013). Cycle slip detection and repair for undifferenced GPS observations under high ionospheric activity. *GPS Solutions*, *17*(2), 247–260. https://doi.org/10.1007/s10291-012-0275-7

Catherine, J., Vijayan, M., Syeda Rabiya, U., Shimna, K., Gahalaut, V. K., & Ramesh, D. (2015). Dichotomy in mode propagation of coseismic ionospheric disturbance: Observations from 11 April 2012 Indian Ocean earthquake. *Journal of Geophysical Research: Space Physics*, *120*(5), 3854–3867. https://doi.org/10.1002/2014ja020621

Chai, Y., & Jin, S. (2021). Two-azimuth co-seismic Ionospheric disturbances following the 2020 Jamaica earthquake from GPS observations. *Journal of Geophysical Research: Space Physics*, *126*(9), e2020JA028995. https://doi.org/10.1029/2020ja028995

Chen, H., Han, P., & Hattori, K. (2022). Recent advances and challenges in the seismo-electromagnetic study: A brief review. *Remote Sensing*, *14*(22), 5893. https://doi.org/10.3390/rs14225893

Chen, J., Zhang, X., Ren, X., Zhang, J., & Zhao, Z. (2020). Ionospheric disturbances detected during a typhoon based on GNSS phase observations: A case study for typhoon Mangkhut over Hong Kong. *Advances in Space Research*, *66*(7), 1743–1753. https://doi.org/10.1016/j.asr.2020.06.006

Chou, M. Y., Cherniak, I., Lin, C. C., & Pedatella, N. (2020). The persistent ionospheric responses over Japan after the impact of the 2011 Tohoku earthquake. *Space Weather*, *18*(4), e2019SW002302. https://doi.org/10.1029/2019sw002302

Chou, M. Y., Yue, J., Lin, C. C., Rajesh, P., & Pedatella, N. (2022). Conjugate effect of the 2011 Tohoku reflected tsunami-driven gravity waves in the ionosphere. *Geophysical Research Letters*, *49*(3), e2021GL097170. https://doi.org/10.1029/2021gl097170

Ciraolo, L., Azpilicueta, F., Brunini, C., Meza, A., & Radicella, S. M. (2007). Calibration errors on experimental slant total electron content (TEC) determined with GPS. *Journal of Geodesy*, *81*(2), 111–120. https://doi.org/10.1007/s00190-006-0093-1

Cowling, D., Webb, H., & Yeh, K. (1971). Group rays of internal gravity waves in a wind-stratified atmosphere. *Journal of Geophysical Research*, *76*(1), 213–220. https://doi.org/10.1029/ja076i001p00213

Crowley, G., Azeem, I., Reynolds, A., Duly, T. M., McBride, P., Winkler, C., & Hunton, D. (2016). Analysis of traveling ionospheric disturbances (TIDs) in GPS TEC launched by the 2011 Tohoku earthquake. *Radio Science*, *51*(5), 507–514. https://doi.org/10.1002/2015rs005907

Dash, P., Panigrahi, B., & Panda, G. (2003). Power quality analysis using S-transform. *IEEE Transactions on Power Delivery*, *18*(2), 406–411. https://doi.org/10.1109/tpwrd.2003.809616

Drob, D. P., Emmert, J. T., Meriwether, J. W., Makela, J. J., Doornbos, E., Conde, M., et al. (2015). An update to the Horizontal Wind Model (HWM): The quiet time thermosphere. *Earth and Space Science*, *2*(7), 301–319. https://doi.org/10.1002/2014ea000089

Drobzheva, V., & Krasnov, V. (2003). The acoustic field in the atmosphere and ionosphere caused by a point explosion on the ground. *Journal of Atmospheric and Solar-Terrestrial Physics*, *65*(3), 369–377. https://doi.org/10.1016/s1364-6826(02)00141-4

Eisenbeis, J., & Occhipinti, G. (2021). The TEC enhancement before seismic events is an artifact. *Journal of Geophysical Research: Space Physics*, *126*(4), e2020JA028733. https://doi.org/10.1029/2020ja028733

Gao, Y., Li, T., Zhou, G., Chen, C.-H., Sun, Y.-Y., Zhang, X., et al. (2023). Acoustic-gravity waves generated by a point source on the ground in a stratified atmosphere-Earth structure. *Geophysical Journal International*, *232*(2), 764–787. https://doi.org/10.1093/gji/ggac364

Ghent, J. N., & Crowell, B. W. (2022). Spectral characteristics of ionospheric disturbances over the southwestern Pacific from the 15 January 2022 Tonga eruption and tsunami. *Geophysical Research Letters*, *49*(20), e2022GL100145. https://doi.org/10.1029/2022gl100145

Haralambous, H., Guerra, M., Chum, J., Verhulst, T. G., Barta, V., Altadill, D., et al. (2023). Multi-instrument observations of various ionospheric disturbances caused by the 6 February 2023 Turkey earthquake. *Journal of Geophysical Research: Space Physics*, *128*(12), e2023JA031691. https://doi.org/10.1029/2023ja031691

Heki, K. (2021). Ionospheric disturbances related to earthquakes. *Ionosphere Dynamics and Applications*, 511–526. https://doi.org/10.1002/9781119815617.ch21

Heki, K. (2024). Decoding multiple source signatures in coseismic ionospheric disturbances of the 2024 January M_w7. 5 Noto-Peninsula earthquake, Central Japan. *Earth and Planetary Science Letters*, *640*, 118796. https://doi.org/10.1016/j.epsl.2024.118796

Heki, K., Bagiya, M. S., & Takasaka, Y. (2022). Slow fault slip signatures in coseismic ionospheric disturbances. *Geophysical Research Letters*, *49*(24), e2022GL101064. https://doi.org/10.1029/2022gl101064

Heki, K., & Ping, J. (2005). Directivity and apparent velocity of the coseismic ionospheric disturbances observed with a dense GPS array. *Earth and Planetary Science Letters*, *236*(3–4), 845–855. https://doi.org/10.1016/j.epsl.2005.06.010

Hines, C. (1972). Gravity waves in the atmosphere. *Nature*, *239*(5367), 73–78. https://doi.org/10.1038/239073a0

Hines, C. (1974). Internal atmospheric gravity waves at ionospheric heights. *The Upper Atmosphere in Motion*, *18*, 248–328. https://doi.org/10.1029/gm018p0248

Huang, C. S. (2016). Plasma drifts and polarization electric fields associated with TID-like disturbances in the low-latitude ionosphere: C/NOFS observations. *Journal of Geophysical Research: Space Physics*, *121*(2), 1802–1812. https://doi.org/10.1002/2015ja022201

Huang, Y., Helmboldt, J., Park, J., Pedersen, T., & Willemann, R. (2019). Ionospheric detection of explosive events. *Reviews of Geophysics*, *57*(1), 78–105. https://doi.org/10.1029/2017rg000594

Huba, J., Drob, D., Wu, T. W., & Makela, J. (2015). Modeling the ionospheric impact of tsunami-driven gravity waves with SAMI3: Conjugate effects. *Geophysical Research Letters*, *42*(14), 5719–5726. https://doi.org/10.1002/2015gl064871

Inchin, P., Snively, J., Zettergren, M., Komjathy, A., Verkhoglyadova, O., & Tulasi Ram, S. (2020). Modeling of ionospheric responses to atmospheric acoustic and gravity waves driven by the 2015 Nepal 7.8 Gorkha earthquake. *Journal of Geophysical Research: Space Physics*, *125*(4), e2019JA027200. https://doi.org/10.1029/2019ja027200

Jin, S. (2018). Two-mode ionospheric disturbances following the 2005 Northern California offshore earthquake from GPS measurements. *Journal of Geophysical Research: Space Physics*, *123*(10), 8587–8598. https://doi.org/10.1029/2017ja025001

Jin, S., Jin, R., & Li, D. (2017). GPS detection of ionospheric Rayleigh wave and its source following the 2012 Haida Gwaii earthquake. *Journal of Geophysical Research: Space Physics*, *122*(1), 1360–1372. https://doi.org/10.1002/2016ja023727

Jin, S., Jin, R., & Li, J. (2014). Pattern and evolution of seismo-ionospheric disturbances following the 2011 Tohoku earthquakes from GPS observations. *Journal of Geophysical Research: Space Physics*, *119*(9), 7914–7927. https://doi.org/10.1002/2014ja019825

Jin, S., Occhipinti, G., & Jin, R. (2015). GNSS ionospheric seismology: Recent observation evidences and characteristics. *Earth-Science Reviews*, *147*, 54–64. https://doi.org/10.1016/j.earscirev.2015.05.003

Krasnov, V., Pelenitcin, G., Ryaskov, O., & Salikhov, N. (1991). Model of ionospheric response on surface industrial explosions. *Vestnik of Academy of Science of Kazakh USR*, *8*, 44–49.

Kundu, S., & Bagiya, M. S. (2024). Investigation of co-seismic ionospheric perturbations generated by shallow earthquakes in the Chile subduction zone. *Journal of Geophysical Research: Space Physics*, *129*(10), e2024JA032676. https://doi.org/10.1029/2024ja032676

Lay, E. H., Parker, P. A., Light, M., Carrano, C. S., Debchoudhury, S., & Haaser, R. A. (2018). Midlatitude ionospheric irregularity spectral density as determined by ground-based GPS receiver networks. *Journal of Geophysical Research: Space Physics*, *123*(6), 5055–5067. https://doi.org/10.1029/2018ja025364

Lay, E. H., Shao, X. M., Kendrick, A. K., & Carrano, C. S. (2015). Ionospheric acoustic and gravity waves associated with midlatitude thunderstorms. *Journal of Geophysical Research: Space Physics*, *120*(7), 6010–6020. https://doi.org/10.1002/2015ja021334

Liu, J., Zhang, X., Yang, X., Yang, M., Zhang, T., Bao, Z., et al. (2023). The analysis of lithosphere–atmosphere–ionosphere Coupling Associated with the 2022 Luding Ms6. 8 earthquake. *Remote Sensing*, *15*(16), 4042. https://doi.org/10.3390/rs15164042

Liu, J. Y., Chen, C. H., Lin, C. H., Tsai, H. F., Chen, C. H., & Kamogawa, M. (2011). Ionospheric disturbances triggered by the 11 March 2011 M9. 0 Tohoku earthquake. *Journal of Geophysical Research*, *116*(A6). https://doi.org/10.1029/2011ja016761

Liu, T. (2023). *Ionospheric disturbances induced by typical special events and their effects on GNSS* (Doctor PhD thesis). Haibin Institute of Technology.

Liu, T., Jiang, Y., Ma, Y., Yu, Z., & Xu, G. (2022). Maximum eigenvalue detection for local ionospheric anomaly-theory, cases, statistics, and potential application. *Measurement*, *203*, 111990. https://doi.org/10.1016/j.measurement.2022.111990

Liu, T., Yu, Z., Ding, Z., Nie, W., & Xu, G. (2021). Observation of ionospheric gravity waves introduced by thunderstorms in low latitudes China by GNSS. *Remote Sensing*, *13*(20), 4131. https://doi.org/10.3390/rs13204131

Ma, Y., Liu, T., Xu, G., & Lu, Z. (2022). Apparent short-period GNSS-ZTD disturbance correlated with Precipitation events. *IEEE Geoscience and Remote Sensing Letters*, *19*, 1–5. https://doi.org/10.1109/lgrs.2022.3210116

Maletckii, B., & Astafyeva, E. (2024). Near-real-time identification of the source of ionospheric disturbances. *Journal of Geophysical Research: Space Physics*, *129*(11), e2024JA032664. https://doi.org/10.1029/2024ja032664

Maletckii, B., Astafyeva, E., Sanchez, S., Kherani, E., & De Paula, E. (2023). The 6 February 2023 Türkiye earthquake sequence as detected in the ionosphere. *Journal of Geophysical Research: Space Physics*, *128*(9), e2023JA031663. https://doi.org/10.1029/2023ja031663

Martinis, C., Baumgardner, J., Wroten, J., & Mendillo, M. (2011). All-sky imaging observations of conjugate medium-scale traveling ionospheric disturbances in the American sector. *Journal of Geophysical Research*, *116*(A5), A05326. https://doi.org/10.1029/2010ja016264

Martire, L., Brissaud, Q., Lai, V. H., Garcia, R. F., Martin, R., Krishnamoorthy, S., et al. (2018). Numerical simulation of the atmospheric signature of artificial and natural seismic events. *Geophysical Research Letters*, *45*(21), 12085–12093. https://doi.org/10.1029/2018gl080485

Maruyama, T., & Shinagawa, H. (2014). Infrasonic sounds excited by seismic waves of the 2011 Tohoku-Oki earthquake as visualized in ionograms. *Journal of Geophysical Research: Space Physics*, *119*(5), 4094–4108. https://doi.org/10.1002/2013ja019707

Medvedev, A., Ratovsky, K., Tolstikov, M., Oinats, A., Alsatkin, S., & Zherebtsov, G. (2017). Relation of internal gravity wave anisotropy with neutral wind characteristics in the upper atmosphere. *Journal of Geophysical Research: Space Physics*, *122*(7), 7567–7580. https://doi.org/10.1002/2017ja024103

Meng, X., Ravanelli, M., Komjathy, A., & Verkhoglyadova, O. P. (2022). On the north-south asymmetry of co-seismic ionospheric disturbances during the 16 September 2015 Illapel M8. 3 earthquake. *Geophysical Research Letters*, *49*(8), e2022GL098090. https://doi.org/10.1029/2022gl098090

Meng, X., Vergados, P., Komjathy, A., & Verkhoglyadova, O. (2019). Upper atmospheric responses to surface disturbances: An observational perspective. *Radio Science*, *54*(11), 1076–1098. https://doi.org/10.1029/2019rs006858

Nayak, S., Bagiya, M. S., & Sunil, A. (2022). Spatial manifestation of resonant ionospheric signatures during the 11 March 2011 Tohoku-Oki earthquake. *Advances in Space Research*, *69*(8), 3000–3007. https://doi.org/10.1016/j.asr.2022.01.027

Nickolaenko, A., & Hayakawa, M. (2014). Localized ionospheric disturbance over the earthquake epicentre and modifications of Schumann resonance electromagnetic fields. *Geomatics, Natural Hazards and Risk*, *5*(3), 271–283. https://doi.org/10.1080/19475705.2013.809557

Nie, W., Wang, F., Qiao, Z., Xu, T., Wang, Y., Ye, M., et al. (2024). Ionospheric irregularities coinciding with the 2023 Typhoon Saola: A multi-instrument study. *Journal of Geophysical Research: Space Physics*, *129*(12), e2024JA033043. https://doi.org/10.1029/2024ja033043

Nie, W., Xu, T., Rovira-Garcia, A., Juan Zornoza, J. M., Sanz Subirana, J., González-Casado, G., et al. (2018). Revisit the calibration errors on experimental slant total electron content (TEC) determined with GPS. *GPS Solutions*, *22*(3), 1–11. https://doi.org/10.1007/s10291-018-0753-7

Nina, A., Pulinets, S., Biagi, P. F., Nico, G., Mitrović, S. T., Radovanović, M., & Popović, L. C. (2020). Variation in natural short-period ionospheric noise, and acoustic and gravity waves revealed by the amplitude analysis of a VLF radio signal on the occasion of the Kraljevo earthquake (Mw= 5.4). *Science of the Total Environment*, *710*, 136406. https://doi.org/10.1016/j.scitotenv.2019.136406

Oinats, A. V., Nishitani, N., Ponomarenko, P., Berngardt, O. I., & Ratovsky, K. G. (2016). Statistical characteristics of medium-scale traveling ionospheric disturbances revealed from the Hokkaido East and Ekaterinburg HF radar data. *Earth, Planets and Space*, *68*, 1–13. https://doi.org/10.1186/s40623-016-0390-8

Padokhin, A., Andreeva, E., Nazarenko, M., & Kalashnikova, S. (2022). Phase-difference approach for GNSS global ionospheric total electron content mapping. *Radiophysics and Quantum Electronics*, *65*(7), 481–495. https://doi.org/10.52452/00213462_2022_65_07_527

Perevalova, N., Sankov, V., Astafyeva, E., & Zhupityaeva, A. (2014). Threshold magnitude for ionospheric TEC response to earthquakes. *Journal of Atmospheric and Solar-Terrestrial Physics*, *108*, 77–90. https://doi.org/10.1016/j.jastp.2013.12.014

Putra, M., Cahyadi, M., Muslim, B., Muafiry, I., & Wulansari, M. (2023). Analysis of tsunami traveling ionospheric disturbances due to tsunami using the GNSS-TEC method. *Paper presented at the IOP Conference Series: Earth and Environmental Science*, *1127*(1), 012003. https://doi.org/10.1088/1755-1315/1127/1/012003

Reddy, C., & Seemala, G. K. (2015). Two-mode ionospheric response and Rayleigh wave group velocity distribution reckoned from GPS measurement following Mw 7.8 Nepal earthquake on 25 April 2015. *Journal of Geophysical Research: Space Physics*, *120*(8), 7049–7059. https://doi.org/10.1002/2015ja021502

Rolland, L. M., Lognonné, P., Astafyeva, E., Kherani, E. A., Kobayashi, N., Mann, M., & Munekane, H. (2011). The resonant response of the ionosphere imaged after the 2011 off the Pacific coast of Tohoku Earthquake. *Earth, planets and space*, *63*(7), 853–857. https://doi.org/10.5047/eps.2011.06.020

Rolland, L. M., Lognonné, P., & Munekane, H. (2011). Detection and modeling of Rayleigh wave induced patterns in the ionosphere. *Journal of Geophysical Research*, *116*(A5), A05320. https://doi.org/10.1029/2010ja016060

Rolland, L. M., Vergnolle, M., Nocquet, J. M., Sladen, A., Dessa, J. X., Tavakoli, F., et al. (2013). Discriminating the tectonic and non-tectonic contributions in the ionospheric signature of the 2011, Mw7. 1, dip-slip Van earthquake, Eastern Turkey. *Geophysical Research Letters*, *40*(11), 2518–2522. https://doi.org/10.1002/grl.50544

Sanchez, S. A., Kherani, E. A., Astafyeva, E., & de Paula, E. R. (2022). Ionospheric disturbances observed following the ridgecrest earthquake of 4 July 2019 in California, USA. *Remote Sensing*, *14*(1), 188.

Savastano, G., Komjathy, A., Verkhoglyadova, O., Mazzoni, A., Crespi, M., Wei, Y., & Mannucci, A. J. (2017). Real-time detection of tsunami ionospheric disturbances with a stand-alone GNSS receiver: A preliminary feasibility demonstration. *Scientific Reports*, *7*(1), 46607. https://doi.org/10.1038/srep46607

Sripathi, S., Singh, R., Tiwari, P., & Kumar, M. R. (2020). On the co-seismic ionospheric disturbances (CIDs) in the rapid run ionosonde observations over Allahabad following Mw 7.8 Nepal Earthquake on April 25, 2015. *Journal of Geophysical Research: Space Physics*, *125*(1), e2019JA027001. https://doi.org/10.1029/2019ja027001

Srivastava, S., Chandran, A., Manta, F., & Taisne, B. (2021). GNSS TEC-based detection and analysis of acoustic-gravity waves from the 2012 Sumatra double earthquake sequence. *Journal of Geophysical Research: Space Physics*, *126*(6), e2020JA028507. https://doi.org/10.1029/2020ja028507

Tachema, A., Kheloufi, N., & Mohamed, E. K. (2024). Investigating ionospheric disturbances as potential seismic precursors: A case study of the 2021 Béjaïa Mw 6.0 earthquake, in Northeastern Algeria. *Journal of the Indian Society of Remote Sensing*, 1–16.

Tang, L., Zheng, K., & Li, X. (2017). Analysis of geometry-free residuals in case of traveling ionosphere disturbances and their impact cycle slip detection. *GPS Solutions*, *21*(3), 1221–1226. https://doi.org/10.1007/s10291-017-0606-9

Thomas, D., Bagiya, M. S., Hazarika, N. K., & Ramesh, D. (2022). On the Rayleigh wave induced ionospheric perturbations during the Mw 9.0 11 March 2011 Tohoku-Oki earthquake. *Journal of Geophysical Research: Space Physics*, *127*(7), e2021JA029250. https://doi.org/10.1029/2021ja029250

Tsugawa, T., Saito, A., Otsuka, Y., Nishioka, M., Maruyama, T., Kato, H., et al. (2011). Ionospheric disturbances detected by GPS total electron content observation after the 2011 off the Pacific coast of Tohoku Earthquake. *Earth, planets and space*, *63*(7), 875–879. https://doi.org/10.5047/eps.2011.06.035

Vadas, S. L. (2007). Horizontal and vertical propagation and dissipation of gravity waves in the thermosphere from lower atmospheric and thermospheric sources. *Journal of Geophysical Research*, *112*(A6), A06305. https://doi.org/10.1029/2006ja011845

Vadas, S. L., Zhao, J., Chu, X., & Becker, E. (2018). The excitation of secondary gravity waves from local body forces: Theory and observation. *Journal of Geophysical Research: Atmospheres*, *123*(17), 9296–9325. https://doi.org/10.1029/2017jd027970

Ventosa, S., Simon, C., Schimmel, M., Dañobeitia, J. J., & Mànuel, A. (2008). The *S*-transform from a wavelet point of view. *IEEE Transactions on Signal Processing*, *56*(7), 2771–2780. https://doi.org/10.1109/tsp.2008.917029

Yanagisawa, H., Abe, I., & Baba, T. (2024). What was the source of the nonseismic tsunami that occurred in Toyama Bay during the 2024 Noto Peninsula earthquake. *Scientific Reports*, *14*(1), 18245. https://doi.org/10.1038/s41598-024-69097-w

Yang, H., Hernández-Pajares, M., Jarmołowski, W., Wielgosz, P., Vadas, S. L., Colombo, O. L., et al. (2022). Systematic detection of anomalous ionospheric perturbations above LEOs from GNSS POD data including possible tsunami signatures. *IEEE Transactions on Geoscience and Remote Sensing*, *60*, 1–23. https://doi.org/10.1109/tgrs.2022.3182885

Zhang, B., Gao, Y., Liu, T., Xu, X., Xu, G., Lu, Z., et al. (2024). Shallow crustal deformation in the Yunnan-Myanmar and surrounding areas by regionally weighted interpolation of GPS measurements data. *Advances in Space Research*, *74*(1), 211–222. https://doi.org/10.1016/j.asr.2024.03.075